https://doi.org/10.5194/egusphere-2026-1974
Preprint. Discussion started: 15 April 2026

How rain shapes cloud-scale dynamics and mass flux in the trades

Florian Poydenot[1], Nina Robbins-Blanch[1,2], Zeen Zhu[3], and Raphaela Vogel[1]

[1]Meteorology, Department of Earth System Sciences, University of Hamburg, Hamburg, Germany
[2]International Max Planck Research School on Earth System Modelling, Max Planck Institute for Meteorology, Hamburg, Germany
[3]Environmental and Climate Sciences Department, Brookhaven National Laboratory, Upton, NY, USA

Correspondence: Florian Poydenot (florian.poydenot@uni-hamburg.de)

Abstract. Trade wind cumuli often precipitate, but the effect of rain processes on their dynamics and organization is still poorly understood. Previous observations of the vertical wind inside clouds were limited to non-precipitating conditions because the mean Doppler velocity from cloud radars is dominated by hydrometeor motion in precipitating clouds. Here, we retrieve the vertical air motion inside precipitating clouds by using the Doppler velocity spectrum from the ground-based Ka-band radars at the Barbados Cloud Observatory. We validate it against available lidar measurements. We combine the in-cloud radar-derived wind with lidar observations outside of clouds into a unified dataset spanning six years (2019-2025) at high (2s) resolution. We show that precipitating cumuli act as shallow squall lines, as predicted by recent large-eddy simulations. These clouds feature a narrow updraft at the gust front that develops up to cloud top. The wider precipitation downdraft is triggered slightly below cloud top, where the rain content is large enough, and extends down to the surface where it forms a cold pool. We show that updrafts and downdrafts contribute nearly equally to the cloud base mass flux. Their balance hinges on the downdraft intensity, likely controlled by microphysical processes. These observations can improve our understanding of tropical convection, shed light on the assumptions behind convective parameterizations and constrain cloud-resolving simulations.

1 Introduction

Rain processes are often underrepresented in our understanding of the trade-wind layer, despite trade cumuli precipitating 30% of the time (Nuijens et al., 2018). Conceptual models of the tropics include clouds through the mass flux, M, they transport in and out of the boundary layer (Arakawa and Schubert, 1974). Rain processes in these models are very simplified (Emanuel, 2019), and models of the trade-wind layer treat shallow convection as non-precipitating (Neggers et al., 2006; Naumann et al., 2019; Albright et al., 2023). The contribution of shallow precipitating clouds is so far poorly characterized due to a lack of suitable observations of the vertical air motion at the cloud scale. Lidars cannot penetrate deeply into clouds, and hydrometeor fall speeds dominate the mean Doppler velocity from cloud-profiling radars. Here, we seek to retrieve the vertical wind in precipitating clouds using established ground-based remote sensing techniques and answer two tightly related questions: what is the vertical circulation at the cloud scale induced by rain? And what is the effect of this circulation on the cloud base mass flux?

Previous estimates of M and its relationship to cloudiness were either done with aircraft passes through clouds (Zipser and LeMone, 1980; LeMone and Zipser, 1980) or remote sensing at ground observatories limited to non-precipitating conditions (Lamer and Kollias, 2015; Klingebiel et al., 2021). In precipitating convection in the trades, rain is produced in updrafts and falls in downdrafts (Malkus, 1955). Once rain reaches the subcloud layer, it evaporates and can create a cold pool, a density current whose gust front can in turn trigger new updrafts (Byers et al., 1949; Vogel et al., 2021; Touzé-Peiffer et al., 2022). Large-eddy simulations (LES) can resolve rain evaporation and cold pools, but the effect of these on convective organization and cloud cover remains unclear (Seifert and Heus, 2013; Lamaakel and Matheou, 2022; Narenpitak et al., 2023; Janssens et al., 2023). On the other hand, recent LES have shown that precipitating trade cumuli act as "shallow squall lines" or "shallow mesoscale convective systems", both in idealized simulations (Alinaghi et al., 2025) and case studies validated against campaign observations (Li et al., 2014; Dauhut et al., 2023). These shallow squall lines are organized very similarly to deep convective systems in which the updraft, downdraft and cold pool are tighly coupled (Houze, 2018). However, observations to validate the simulations were limited to the atmospheric thermodynamic properties and the cloud field morphology, and the in-cloud circulation itself has not been observationally resolved yet.

Inside precipitating clouds, the vertical air motion can be estimated from the radar Doppler spectrum, either by estimating the vertical motion of droplets of a given size and correcting for their fall speed, or by retrieving the entire drop size distribution (DSD) from Doppler velocity spectra from one or multiple frequencies, in which the vertical air motion appears as a fitting parameter to this inverse problem (Moisseev and Chandrasekar, 2007; Tridon and Battaglia, 2015; Battaglia et al., 2016; Tridon et al., 2017). Methods that look at the motion of a single class of droplets notably include measuring the position of Mie resonances in the W- or G-band spectrum to obtain the vertical speed of droplets in the millimeter range (Lhermitte, 1988; Kollias et al., 2002; Yurk et al., 2025). Likewise, the slow falling edge of the Doppler velocity spectrum, V_{edge}, just above the noise level, can be used as a proxy for vertical motion by assuming that only cloud droplets with a negligible fall speed contribute to it (Battan and Theiss, 1966; Shupe et al., 2008). However, V_{edge} must be corrected for turbulence broadening and the limit of detection set by the signal-to-noise ratio at a given range gate and hydrometeor backscattered power. (Zhu et al., 2021) developed such a retrieval for stratocumulus decks on Graciosa Island in the Azores archipelago, which was latter applied to shallow cumuli there (Jeong et al., 2022). Conditions in the Azores are extratropical (Rémillard and Tselioudis, 2015) and mesoscale cloud organization patterns there differ from the tropics (Schulz et al., 2021), and so the question of in-cloud dynamics in the trades closer to the intertropical convergence zone remains.

We use the Zhu et al. (2021) method and lidar observations to retrieve the vertical wind over a six-years period of trade-wind cumuli and congestus at the Barbados Cloud Observatory (BCO). The BCO, its instruments and the retrievals used are presented in section 2. In Section 3 the new dataset is used to study the precipitating cloud life cycle and its spatial organization at the cloud scale. The resulting mass flux of precipitating convection and its controls are quantified in Section 4. Conclusions are presented in Section 5.

https://doi.org/10.5194/egusphere-2026-1974
Preprint. Discussion started: 15 April 2026

2 Methods

2.1 The Barbados Cloud Observatory

The Barbados Cloud Observatory (BCO), located on the windward coast of the island of Barbados in the West Indies at $13°9'45.5''$N, $59°25'43.5''$W, has been operating continuously with a large variety of instruments since 2010 (Stevens et al., 2016), and is representative of the average conditions in the trades (Medeiros and Nuijens, 2016). Radar Doppler spectra are available from two vertically-pointing Ka-band radars at $2\,\mathrm{s}$ temporal and $31\,\mathrm{m}$ vertical resolution with 512 spectral bins spanning $\pm 10.7\,\mathrm{m/s}$ (Görsdorf et al., 2015). The MBR2 (Metek MIRA 35) radar operated at this resolution between May 2018 and September 2024, after which it was decommissioned. Due to processing issues, only the data obtained after August 2019 is used. The MBRS (Metek MIRA 35S) radar replaced the MBR2 and operates since January 2023.

We also use the two wind lidars operated at the BCO, both HALO Photonics StreamLine Pro Scanning Doppler Lidars (Päschke et al., 2015). The first one, WindLidar1, was operated in vertically-pointing mode between March 2016 and October 2019, then between July 2021 and September 2024, and again since September 2025. The second one, WindLidar2, recorded VAD scans between March 2019 and July 2021. It then operated in vertically-pointing mode between September 2024 and September 2025. VAD scans measure the vertical velocity at $10\,\mathrm{s}$ and $15\,\mathrm{m}$ resolution, vertically-pointing lidars at $1.3\,\mathrm{s}$ and $15\,\mathrm{m}$ resolution.

2.2 Radar retrieval of the vertical wind

The vertical air motion is retrieved following (Zhu et al., 2021). The velocity at the slow falling edge of the spectrum V_{edge} is assumed to be the velocity of the cloud droplets in the radar volume. The cloud droplets are assumed to have zero fallspeed, so that their velocity is the air velocity w. However, the position of the slow falling edge depends also on the spectral broadening due to turbulence and shear (a broader spectrum will have signal at higher spectral lines) and the signal-to-noise ratio (SNR), with the latter being the dominant factor. For the same air motion, a higher SNR means that the slow falling edge will be displaced towards higher velocities. The air motion is obtained as

$$w = V_{\mathrm{edge}} - \sigma_t - \sigma_{sm} - \delta_{\mathrm{SNR}}. \quad (1)$$

V_{edge} is measured from the spectra corrected for folding. The turbulence broadening σ_t and the shear broadening σ_{sm} are estimated following (Borque et al., 2016) and (Zhu et al., 2021). The SNR correction δ_{SNR} is taken from (Zhu et al., 2021), except in the cloud pixels below $500\,\mathrm{m}$ and $0\,\mathrm{dB}$. There we perform a phenomenological correction $\delta_{\mathrm{SNR}} = 0.04\sqrt{\mathrm{SNR}+39}[\mathrm{m/s}]$ instead, which is obtained after comparison with the lidars. Values from the MBRS at all range gates are further corrected by $-0.12\,\mathrm{m/s}$ (three spectral lines) for better agreement with the MBR2 and the lidar (Figure A1a). After correction, the two radars agree within $\pm 0.1\,\mathrm{m/s}$ of each other during the period when they both operated at the same time (March 2023-March 2024). Figure 1c shows the retrieved vertical motion inside a typical precipitating cloud. The mean Doppler radar velocity V_d and the retrieved wind markedly differ in the precipitation downdraft, where V_d closely mirrors the reflectivity (Figure 1a),

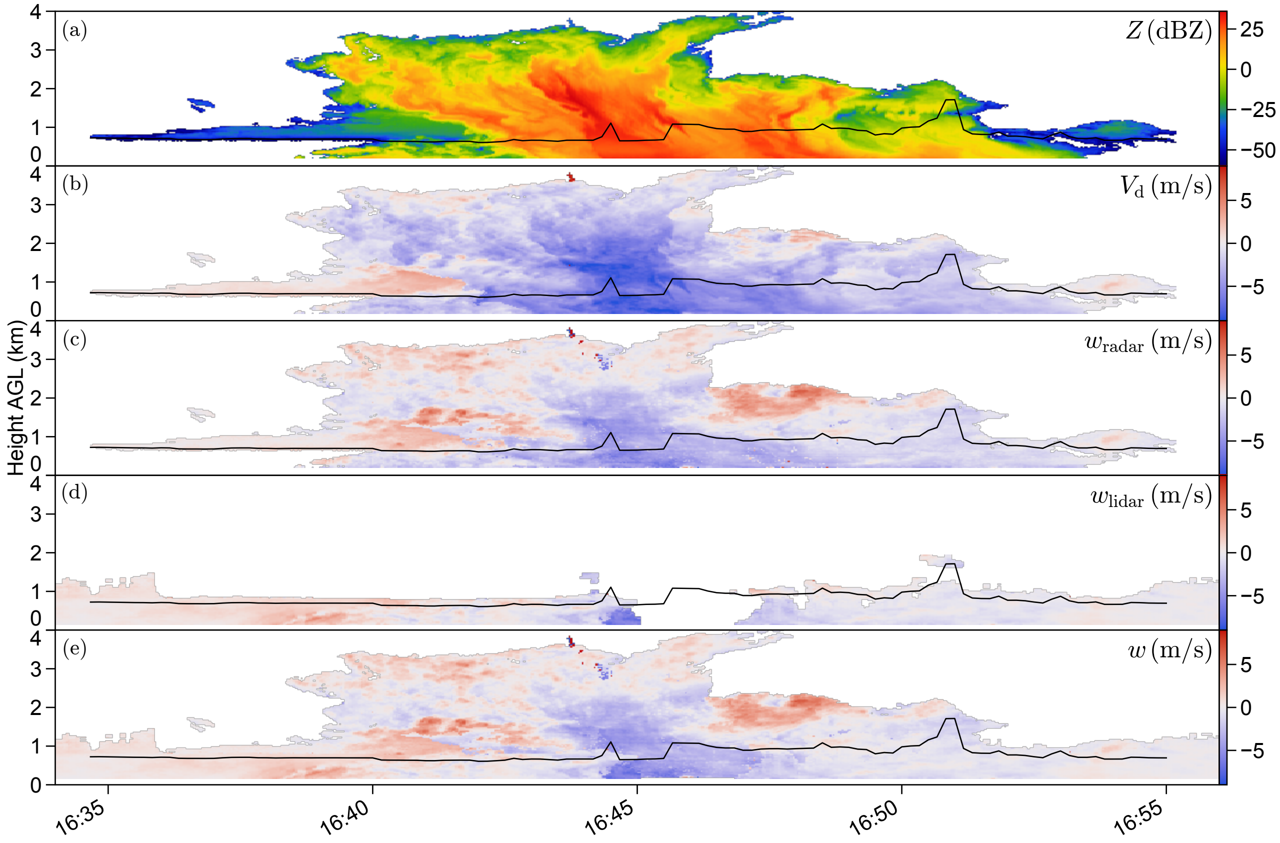

Figure 1. Example rain event on 2024-09-15. (a) Ka-band radar reflectivity. (b) Mean radar Doppler velocity V_d. (c) Radar-only retrieval w_radar. (d) Doppler lidar measurements w_lidar. (e) Lidar-radar composite of the vertical wind w. Solid black lines: ceilometer cloud base height.

while the vertical wind does not vary much inside the downdraft. The retrieval also unveils regions of upwards motion absent from V_d (Figure 1b, c). Notably, an updraft starts at the gust front and extends up to cloud top.

We evaluate the consistency of the retrieval by comparing w and V_d. Figure 2 shows the histogram of the pixel-based joint distribution of mean Doppler radar velocity V_d with retrieved vertical wind w. Since V_d is weighted by the sixth power of the droplet diameter, it reflects the motion of drizzle or rain droplets as soon as they are present in the radar volume. This leads to the constraint that V_d cannot be larger than w: data in the half of the graph $V_d > w$ is therefore unphysical. Very few pixels (around $0.5\,\%$ of the total) fall into that region. Updrafts ($w > 0$) can be correctly featured both when droplets moving upwards along with the air ($V_d > 0$) or when falling downwards ($V_d < 0$). The retrieval also performs in a consistent way in downdrafts ($w < 0$), the majority of which feature the air moving slower than the droplets ($V_d < w$). Since the retrieval assumes the presence of cloud droplets, it can overcorrect V_edge when they fully evaporate in downdrafts below cloud base, but this effect remains limited ($3\,\%$ of the total).

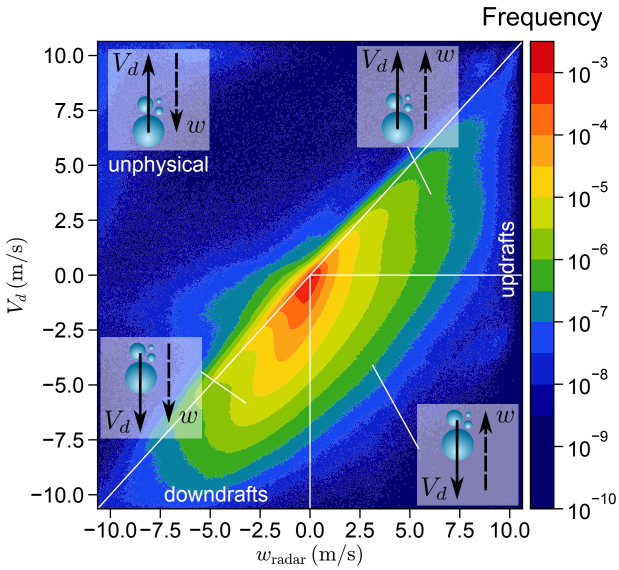

Figure 2. Histogram of the pixel-based joint distribution of mean Doppler radar velocity V_d with vertical wind w. $w > 0$ is updrafts, either rain-free ($V_d > 0$) or in rain ($V_d < 0$). $w < 0$ corresponds to downdrafts. Data in the $V_d > w$ half of the graph is unphysical.

The Doppler wind lidars at the BCO also measure vertical velocities, albeit only in the presence of scatterers and without large droplets that quickly attenuate the signal. Observations are thus limited to the subcloud layer, near cloud base and around the edges of optically thin clouds, in the absence of rain. Lidar and radar-derived vertical air velocities are overall within $0.2\,\mathrm{m/s}$ of each other (Figure A1b). This bias remains acceptable for the majority of pixels below $15\,\mathrm{dB}$ around typical cloud base heights ($500-800\,\mathrm{m}$) and for the visible pixels in the cloud layer (Figure A1c). At higher SNR in the subcloud layer, the retrieval tends to overcorrect for downward motion.

2.3 Composite radar-lidar vertical velocity and cloud segmentation

To get a best estimate of the vertical motion both in the cloud and subcloud layers, we thus merge lidar measurements with the radar retrieval, similar to Jeong et al. (2022). We first coarsen the lidar to the lower radar resolution. Between the surface up to $623\,\mathrm{m}$, we only take the lidar measurement. Between $623\,\mathrm{m}$ and $2000\,\mathrm{m}$, we take the weighted average of the lidar and the radar, the lidar weight being 1 at $623\,\mathrm{m}$ and linearly decreasing to 0 at $2000\,\mathrm{m}$. Above, we only use the radar. If the lidar value is not available, we take the radar one. Figure 1d shows what the lidar typically measures in such a rain event; Figure 1e is the outcome of the lidar-radar compositing. The main differences are at the gust front near 1640 UTC, where the small apparently downward motion is corrected upwards. Note that here, the downdraft velocity as seen by the lidar near the surface is higher than retrieved from the radar.

Clouds are segmented and classified using the algorithm by (Konow, 2020). We further divide the cloud population into non-precipitating clouds, where the maximal radar reflectivity is below $-15\,\mathrm{dBZ}$ across the whole cloud, and precipitating

https://doi.org/10.5194/egusphere-2026-1974
Preprint. Discussion started: 15 April 2026

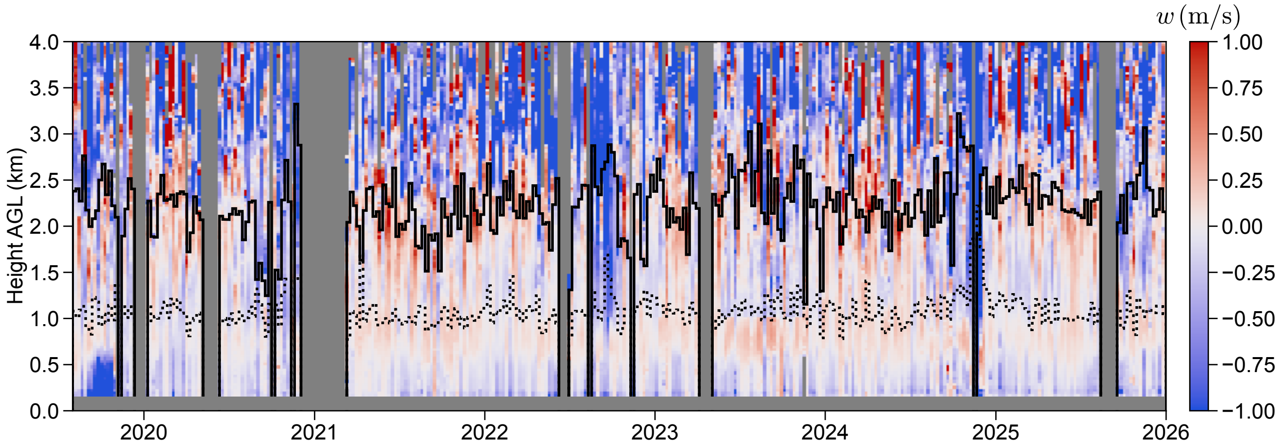

Figure 3. 7-day mean vertical velocity inside both precipitating and non-precipitating clouds. Gray: no data. Dotted black line: mean cloud top height of non-precipitating clouds. Solid black line: mean cloud top height of precipitating clouds.

clouds where the maximal reflectivity is above $-15\,\mathrm{dBZ}$. Similar thresholds have previously been used in the literature (Frisch et al., 1995; Liu et al., 2008; Ghate et al., 2011; Lamer and Kollias, 2015). Clouds with a top height above $4.5\,\mathrm{km}$ are discarded, as the retrieval assumes that only liquid water droplets are present. The descriptive statistics of the segmented populations are summarized in Table A1. This classification solely by the reflectivity includes potentially ambiguous cases of drizzle and/or virga as precipitating (Kalesse-Los et al., 2023; Roschke et al., 2025). Since our focus here is on in-cloud motion and not surface precipitation, the threshold of $-15\,\mathrm{dBZ}$ is chosen to differentiate between drizzle-dominated clouds in which the mean Doppler velocity is biased by these faster-falling droplets, and clouds for which that is not the case. Inside non-precipitating clouds, the (Zhu et al., 2021) retrieval is biased, as it assumes the presence of drizzle or rain drops. However, (Klingebiel et al., 2021) have shown for these clouds that the mean Doppler radar velocity is unbiased with regards to the lidar measurements. Therefore, for non-precipitating clouds, we take as the vertical wind the lidar velocity, or the mean Doppler radar velocity if the lidar observation is not available.

In total, we retrieved $42898\,\mathrm{h}$ of data, spanning more than six years (August 2019-December 2025). Figure 3 shows the 7-days mean velocity, inside both precipitating and non-precipitating clouds.

3 Circulations at the cloud scale

3.1 The relative contribution of precipitating clouds to the total vertical motion

Figure 4 shows the average vertical velocity for both non-precipitating and precipitating clouds. Non-precipitating clouds feature mean upward motion through the entire depth of their cloud layer, while mean ascending motion is only found in precipitating clouds near cloud top. Here, we define updrafts as all pixels with $w > 0$ and downdrafts as all pixels with $w < 0$.

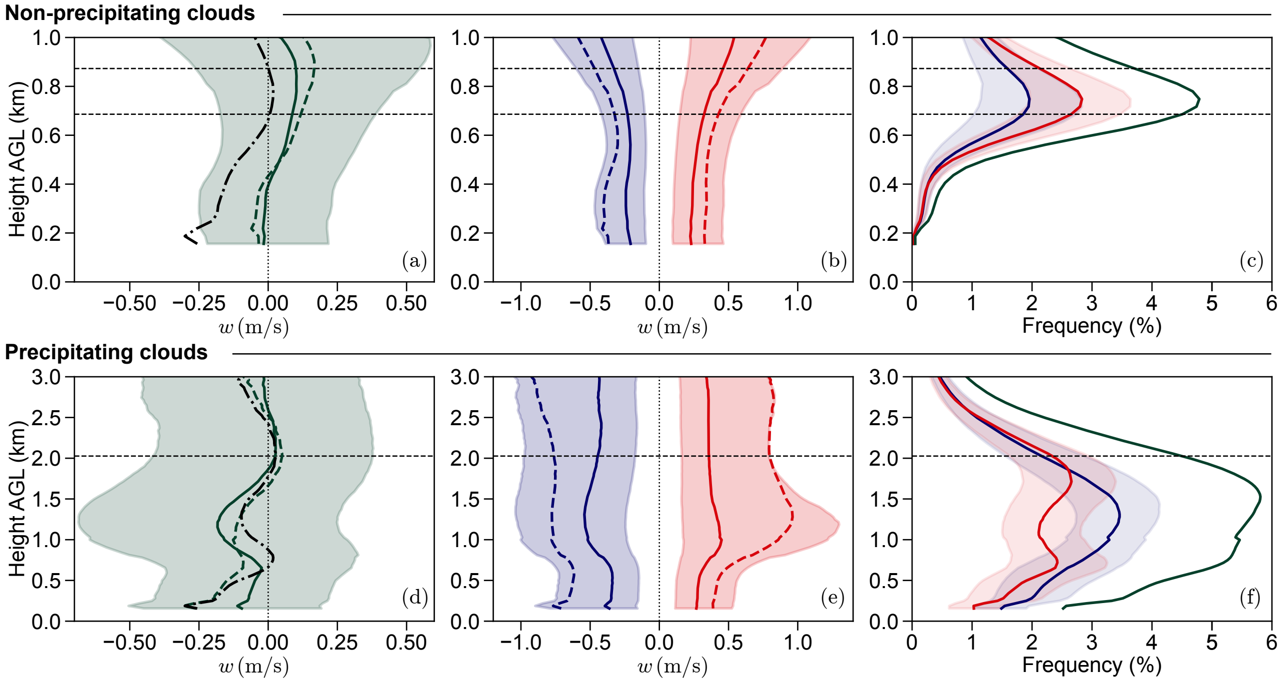

Figure 4. Characteristics of the vertical motion for non-precipitating clouds (top row, a-e, only up to 1 km) and precipitating clouds (bottom row, f-j). Dashed horizontal lines: median cloud top height and cloud base (for non-precipitating clouds only). (a, f) Vertical velocity. Solid green line: median, shading: first-third quartiles, dashed green line: mean, dash-dotted black line: mean for all clouds. (b, g) Velocity of the upwards-moving pixels (red, $w > 0$) and the downwards-moving pixels (blue, $w < 0$). Solid lines: medians, shading: first-third quartiles, dashed lines: means. (c, h) Frequency of upwards-moving (red) and downwards-moving (blue) pixels. Solid green line: total frequency. Shading: retrieval uncertainty.

Updraft and downdraft velocities are very similar in magnitude (Figure 4b, e). Downdraft variability is nearly constant with height, while updrafts have a maximum in variability near $1\,\mathrm{km}$, inside the cloud layer.

The relative distribution of downdrafts and updrafts controls the overall motion (Figure 4c, f). We define the updraft and downdraft frequencies, a_u and a_d, as the fraction of the cloudy pixels with positive or negative w; by construction, $a_u + a_d$ equals the cloud fraction, a (solid green line on Figure 4c, f). The non-precipitating cloud fraction is around $5\,\%$, in line with previous observations at BCO (Medeiros and Nuijens, 2016; Nuijens et al., 2014; Lamer and Kollias, 2015). Precipitating clouds have the same or slightly higher cloud fraction compared to non-precipitating clouds, while previous works show them to comprise only $\sim 30\,\%$ of the low cloud fraction (Nuijens et al., 2018). We explain this apparent discrepancy by our choice of threshold, which aims to differentiate clouds based on whether drizzle drops influence the radar Doppler velocity spectrum, and not based on their surface precipitation.

We further define the relative updraft-to-downdraft fraction

$$f_{\uparrow/\downarrow} = \frac{a_u}{a_u + a_d} \qquad (2)$$

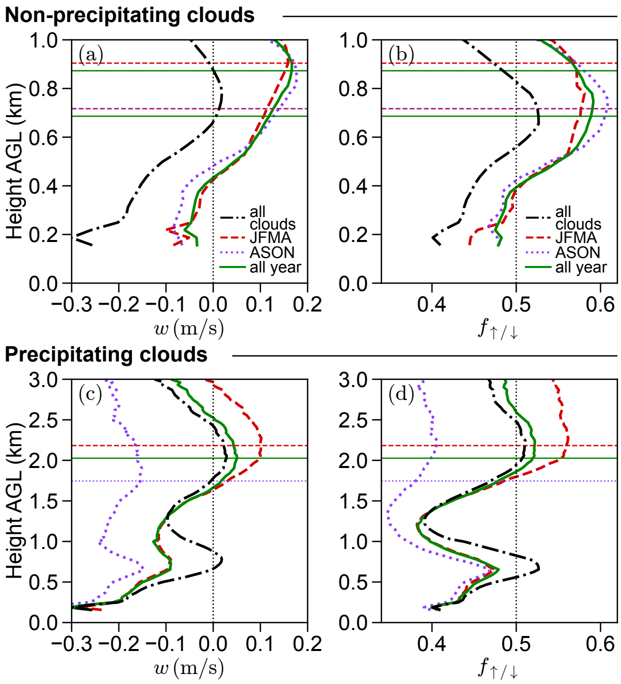

Figure 5. Characteristics and seasonal variability of the vertical motion for non-precipitating clouds (top row, a-b, only up to 1 km) and precipitating clouds (bottom row, c-d). Dashed horizontal lines: median cloud top height and cloud base (for non-precipitating clouds only). (a, c) Mean velocity w. (b, d) Relative updraft-to-downdraft fraction $f_{\uparrow/\downarrow}$. Dashed red lines: winter (JFMA, dry season), dotted purple lines: summer (ASON, wet season), solid green lines: all year. The dash-dotted black line is for all clouds (precipitating and non-precipitating), year-round.

to quantify their relative abundances independently of the cloud fraction. $f_{\uparrow/\downarrow} = 1/2$ means that updrafts and downdrafts occur in equal amounts. Figure 5 shows that non-precipitating clouds feature updrafts nearly $60\,\%$ of the time through their entire depth. In precipitating clouds, updrafts and the mean velocity have a small peak near cloud base, but downdrafts are overall more frequent below $2\,\mathrm{km}$, and make up for up to $60\,\%$ of the motion inside the cloud layer. At cloud top, this reverses and updrafts are again slightly more frequent. Since our non-precipitating and precipitating clouds have similar cloud fractions, they contribute nearly the same to the average for all shallow clouds (dash-dotted black lines on Figures 4 and 5). The average velocity thus has two peaks in both magnitude and updraft frequency, one near cloud base driven mostly by non-precipitating clouds, and one near the trade inversion driven by the top of precipitating cumuli.

Seasonality at the BCO is linked to the migration of the intertropical convergence zone (ITCZ). During the dry winter months (January to April, although the season extends between December and June), subsidence prevails, along with enhanced low-level cloudiness (Brueck et al., 2015). In the wet summer months (August to November, although the season starts in June and ends in December), deep convection is supported by low-level convergence, though the influence of the trades is still felt in Barbados (Stevens et al., 2016). Figure 5 shows that seasonality has little effect on non-precipitating clouds, both in terms of

w and $f_{\uparrow/\downarrow}$. The overall vertical structure of precipitating clouds persists year-round, with a peak in relative updraft frequency and velocity at cloud base and cloud top. However, precipitating clouds in the wet season have both more intense and larger downdrafts than in the dry season, possibly due to the more disturbed conditions in summer. The year-round average closely resembles the winter profile, except near cloud top where updrafts are more frequent in the dry season.

3.2 Cloud depth and the cloud life cycle

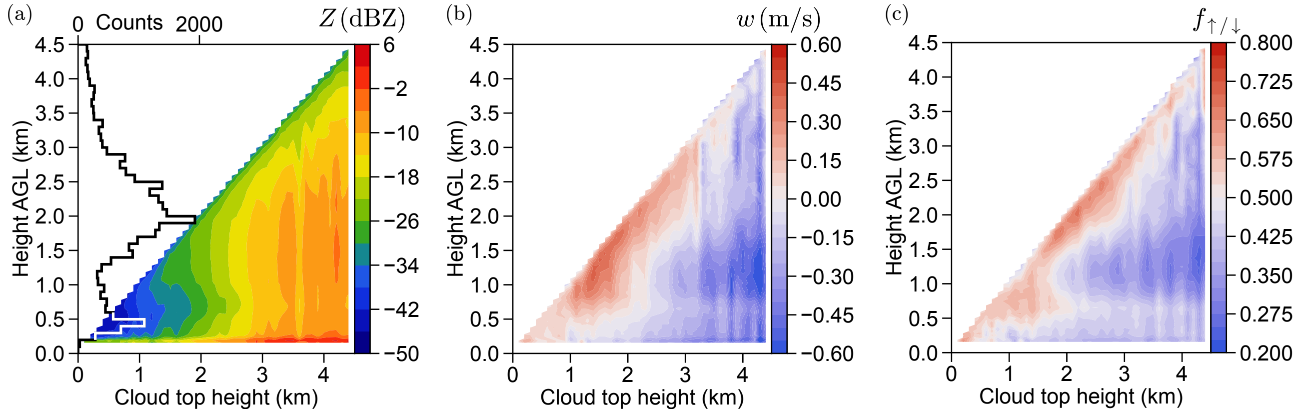

Figure 6. Average vertical profiles of precipitating clouds binned by cloud top height. (a) Average reflectivity Z. Solid black line: histogram of cloud top height. (b) Average in-cloud vertical velocity w. (c) Average relative updraft-to-downdraft fraction $f_{\uparrow/\downarrow}$.

The year-round average picture obscures the variability in vertical velocity associated with clouds of different depths. To account for this variability, we group the 27363 observed precipitating clouds (see Table A1) by their top heights and compute the associated average profiles. Figure 6 shows the average reflectivity Z, velocity w and updraft-to-downdraft fraction $f_{\uparrow/\downarrow}$ by bins of $100\,\mathrm{m}$ of cloud top height (CTH). The CTH distribution peaks near the trade inversion. Deeper clouds are associated with larger reflectivities.

Clouds with tops slightly below $2\,\mathrm{km}$ feature updrafts throughout their entire depth, manifested by both $w > 0$ and $f_{\uparrow/\downarrow} > 1/2$. They have small downdrafts below cloud base, associated with precipitation. Deeper clouds reaching the trade inversion and above feature a region dominated by updrafts just below cloud top, around $500\,\mathrm{m}$ in depth. These clouds are able to generate large, intense downdrafts, extending between the cloud top updraft region and the surface. Downdraft intensity and frequency increases with CTH, while w near cloud top is the largest for CTH around $1.5\,\mathrm{km}$, indicating that these clouds are in their state of fastest development, and $f_{\uparrow/\downarrow}$ is largest near $2\,\mathrm{km}$.

Non-precipitating clouds do not show this altitude-dependent structure: upwards motion is confined to the $0.5-1\,\mathrm{km}$ layer and its intensity does not vary with cloud depth (Figure S2). We hypothesize that the vertical structure of motion inside precipitating clouds corresponds to different life stages of the cloud. Shallow clouds initially near the lifting condensation level rise by latent heat release, allowing for more rain production. When they deepen into the congestus stage (Acquistapace et al., 2026) and reach the trade inversion, their ascent is slowed; simultaneously, they have produced enough rain to generate a large

https://doi.org/10.5194/egusphere-2026-1974
Preprint. Discussion started: 15 April 2026

downdraft by evaporative cooling inside the cloud layer. Positive buoyancy is confined near cloud top where there is latent heat release by condensation. The deepest clouds, above $3\,\mathrm{km}$, mostly contain downdrafts, indicating that they may be decaying. This cloud life cycle is consistent year-round. Summer clouds feature both more intense updrafts and downdrafts, and overall enhanced downwards motion, while winter clouds are close to the all-year average (Figure S1).

3.3 Precipitating trade wind cumuli as shallow squall lines

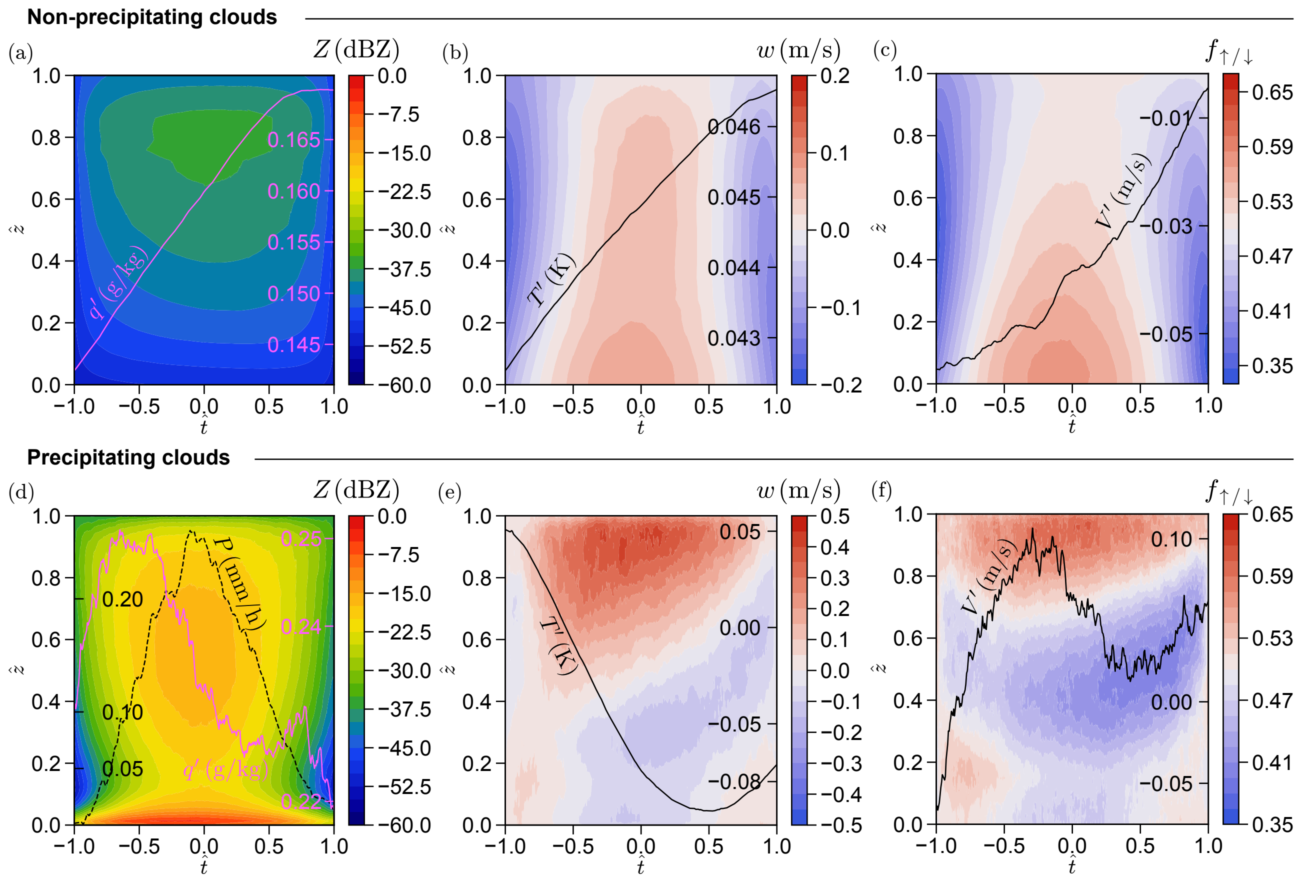

Figure 7. Composite means of non-precipitating (top row, a-c) and precipitating (bottom row, d-f) clouds and the associated surface meteorology anomalies with regards to their daily averages. Velocities include clear air pixels around the clouds (see text). (a, d) Reflectivity Z. Solid pink line: specific humidity anomaly q'. Dashed black line: precipitation rate [(d) only]. (b, e) Vertical velocity w. Solid black line: temperature anomaly T'. (c, f) Relative updraft-to-downdraft fraction $f_{\uparrow/\downarrow}$. Solid black line: wind magnitude anomaly V'. The coordinates are normalized with regards to the lowest range gate and cloud top for the height $\hat{z}$ and the cloud start and end for the time $\hat{t}$. The wind direction is from right to left.

To obtain a statistical picture of the spatial structure of the vertical motion, we composite the 13463 precipitating clouds with echoes detected near the surface, as well as the 653559 non-precipitating clouds (see Table A1). Clouds in time t and height z

https://doi.org/10.5194/egusphere-2026-1974
Preprint. Discussion started: 15 April 2026

are interpolated on a regular 1800×75 $(\hat{t}, \hat{z})$ grid with the reduced time and height

$$\hat{t} = \frac{2t - (t_{\mathrm{cloud\,start}} + t_{\mathrm{cloud\,end}})}{t_{\mathrm{cloud\,end}} - t_{\mathrm{cloud\,start}}}, \tag{3}$$

$$\hat{z} = \frac{z - \mathrm{CBH}}{\mathrm{CTH} - \mathrm{CBH}}, \tag{4}$$

with CBH the cloud base height as defined by the lowest range gate in which echoes are detected, in this section always below $200\,\mathrm{m}$. At the radar resolution, this grid corresponds to $30\,\mathrm{min}$ and $2.5\,\mathrm{km}$, slightly above the mean cloud duration ($19\,\mathrm{min}$) and cloud top height ($2.3\,\mathrm{km}$). Non-precipitating clouds are instead composited on a smaller 900×30 grid to account for their shorter duration ($1\,\mathrm{min}$) and depth ($1\,\mathrm{km}$). We do not limit ourselves to in-cloud pixels only: clear-air motion measured by the lidar within the $(t_{\mathrm{cloud\,start}}, t_{\mathrm{cloud\,end}}) \times (\mathrm{CBH}, \mathrm{CTH})$ box around the cloud is also considered for the compositing. Likewise, we re-grid time series of the surface meteorology during each precipitating cloud, considering the mean rain intensity P, the temperature anomaly T', the moisture anomaly q' and the wind speed magnitude anomaly V' with regards to their $6\,\mathrm{h}$ running averages. Since the wind speed does not vary much at the BCO (mean surface wind speed $\pm 1\sigma$: $5.2 \pm 2.2\,\mathrm{m/s}$), we interpret $\hat{t}$ as a rescaled space coordinate, measuring along the average transect of the clouds.

Figure 7 shows the composite mean Z, w, $f_{\uparrow/\downarrow}$ and the surface quantities. Non-precipitating clouds peak in reflectivity near cloud top, indicating that droplet nucleation and condensational growth are taking place there. The updraft develops/extends through the entire cloud depth. There is a narrow subsiding shell near the cloud edges, most likely extending into clear air as well, as was previously found (Heus and Jonker, 2008; Heus et al., 2009; Wang and Geerts, 2013; Lamer and Kollias, 2015; Hernández Pardo et al., 2025). The surface features a very small but statistically significant hot, moist anomaly, likely linked to the presence of thermals supporting the clouds.

For precipitating clouds, reflectivity is highest near the surface $\hat{z} = 0$ and inside the cloud; the peak in Z also coincides with the peak in surface rain intensity, near the center of the cloud ($\hat{t} = 0, \hat{z} \simeq 0.5$). The vertical motion is asymmetric between the front ($\hat{t} = -1$, downwind) and the back of the cloud ($\hat{t} = 1$, upwind). The updraft extends between the surface and cloud top, where the largest values of w and $f_{\uparrow/\downarrow}$ are found. The precipitation downdraft extends between cloud top at the back of the cloud and the surface. $f_{\uparrow/\downarrow}$ shows that the downdraft is larger everywhere in the cloud layer, and the updraft near the front is narrow and intense. The minimum in $f_{\uparrow/\downarrow}$ on the upwind side, far away from the surface, in a region with no minimum in w and lower Z, is associated with more stratiform downdrafts, less intense in magnitude and containing less rain than the convective core.

At the surface, the composite temperature anomaly shows that the cooling by the downdraft is largest after the rain has peaked. The wind anomaly is largest just before the downdraft, decreases until the temperature anomaly is at its largest, then picks up again to a lower value at the upwind side of the cloud. The moisture anomaly is positive during the entire cloud and varies weakly, but is largest on the downwind side and reaching a minimum near the upwind side. Near the surface, updrafts are found where the two gust fronts are, the most intense one on the downwind side and the less intense one on the upwind side. These updrafts mostly happen in clear air as seen by the very low values of Z there.

This spatial structure shares the characteristics of "shallow mesoscale convective systems" (MCS), also called "shallow squall lines", observed in large-eddy simulations (LES) of the trades (Li et al., 2014; Dauhut et al., 2023; Alinaghi et al., 2025) and named in reference to mesoscale convective systems (Houze, 1977; Houze et al., 1980; Houze, 2018). The convective downdraft, where the largest reflectivities are found, creates a cold pool, whose gust front triggers convection that feeds into the main updraft supplying the system with moisture and buoyancy. At the back of the system, old decaying convective elements make up a stratiform anvil and the associated "mesoscale downdraft", less intense than the convective one. Note that we have not conditioned the compositing on the presence of a surface cold pool, but it still emerges in the mean structure in a way that is in line with previous studies (Vogel et al., 2021).

This shallow MCS organization is fairly robust with regards to the choices made in the compositing. The median fields show lower magnitudes but the same structures (Figure S3). If we do not rescale time and height, but instead apply the transformation $t' = t - t_{Z_{\max}}$ so that the times of maximum reflectivity all line up for every cloud, we find again the same results (Figure S4). Notably, the convective downdraft extending to the surface and the larger, less intense stratiform downdraft appear clearly separated around $10\mathrm{min}$ after the peak in reflectivity. If we composite on the one hand "short" clouds with a duration below 20 minutes, unlikely to have stratiform outflows, and "long" clouds with a duration above, likelier to feature anvils, we find as expected that the large mesoscale downdraft is only really present when the anvil is there (Figures S5-S6). The missing ingredient for a complete description of these systems as shallow MCS is shear. Classical Rotunno-Klemp-Weisman theory (Rotunno et al., 1988; Weisman and Rotunno, 2004) and recent LES of the trades (Helfer et al., 2020; Helfer and Nuijens, 2021) predict that wind shear and cold pool vorticity are in balance for optimal squall line development, leading to tilted updrafts that avoid evaporation and cooling from the precipitation they generate. The slant in Figure 7e might only be an artifact of the averaging, rather than shear, as it is not visible in the median velocity (Figure S3). Further work is needed to understand this effect.

4 The vertical mass flux of precipitating convection

The convective mass flux of clouds is defined as (Arakawa and Schubert, 1974; Emanuel, 1991)

$$M = \rho w a, \tag{5}$$

with ρ the air density, w the average velocity inside the clouds and a the cloud fraction. M can be decomposed into the updraft and downdraft mass fluxes, M_u and M_d, such that

$$M = M_u + M_d = \rho w_u a_u + \rho w_d a_d, \tag{6}$$

with w_u, w_d the updraft and downdraft velocities and a_u, a_d their respective fractions. For simplicity, we take $\rho = 1\,\mathrm{kg.m^{-3}}$. In line with previous studies at the BCO (Lamer and Kollias, 2015; Klingebiel et al., 2021), we measure the mass flux by sampling the average velocities and area fractions over $24\,\mathrm{h}$ periods to minimize the sampling uncertainty and remove the effect of diurnal variability (Vial et al., 2019). We also sample conditionally over each day for non-precipitating clouds only, precipitating clouds only or all shallow clouds to ascertain the effect of rain on M. Excluded clouds are correctly not counted as clear-sky; however, clear-sky does include high anvil clouds with bases above $6.5\,\mathrm{km}$, so that the cloud fractions should be

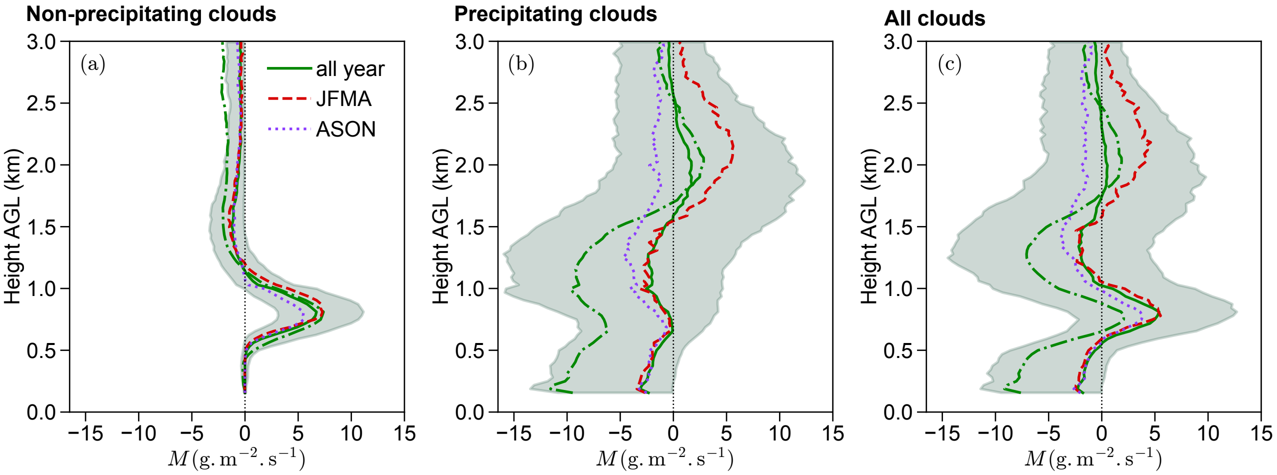

Figure 8. Vertical profiles of in-cloud mass flux sampled over 24 h periods. (a) Non-precipitating clouds. (b) Precipitating clouds. (c) All clouds. Dashed red lines: dry season median (JFMA), dotted purple lines: wet season median (ASON), solid green lines: all year median, dash-dotted green lines: all year mean. Shading: first-third quartiles.

understood as low cloud fractions only. Updrafts and downdrafts are again defined as all pixels with $w > 0$ (resp. $w < 0$). We obtain this way 1689 vertical profiles of the mass flux for each regime, covering a total of 39437 h, the largest dataset to date at this resolution.

Figure 8 presents the mass flux vertical profiles. The non-precipitating cloud mass flux closely resembles previous observations (Ghate et al., 2011; Lamer and Kollias, 2015; Klingebiel et al., 2021), with a peak value of $\sim 6\,\mathrm{g.m^{-2}.s^{-1}}$ at $\sim 810\,\mathrm{m}$, which is just above cloud base. Note that we have not excluded negative mass fluxes here, so decaying clouds do contribute to the statistics. The mass flux of precipitating clouds has a nearly zero median at cloud base, but a negative mean around $-6\,\mathrm{g.m^{-2}.s^{-1}}$ at $\sim 655\,\mathrm{m}$, just below cloud base. M is also much more variable for these clouds, the 25th and 75th quantiles at that height being $-8\,\mathrm{g.m^{-2}.s^{-1}}$ and $3\,\mathrm{g.m^{-2}.s^{-1}}$, respectively. Overall, all clouds combined have a positive mass flux at cloud base of $5\,\mathrm{g.m^{-2}.s^{-1}}$, mainly driven by non-precipitating clouds. Seasonality is mostly present just below cloud top and the trade inversion, with mass flux there as large as at cloud base in the winter and negative in the summer. This seasonality is almost exclusively due to the precipitating clouds.

Previous studies have established that for non-precipitating cumuli, the cloud fraction mainly controls the mass flux, the cloud base velocity only playing a secondary role (Lamer and Kollias, 2015; Klingebiel et al., 2021). Does this mechanism still hold in the presence of precipitation? To investigate this, we average the different vertical profiles between 600 and 900 m to obtain relationships between their values near cloud base. Note that Klingebiel et al. (2021) used instead the maximum near cloud base of each of the profiles, but since we must also consider near zero or negative mass fluxes, this method is not suitable.

Figure 9 presents the different controls on the mass flux. For non-precipitating clouds, we reproduce previous findings (Pearson correlation $r = 0.69$ between M and a, and only $r = 0.38$ between M and w). This no longer holds for precipitating

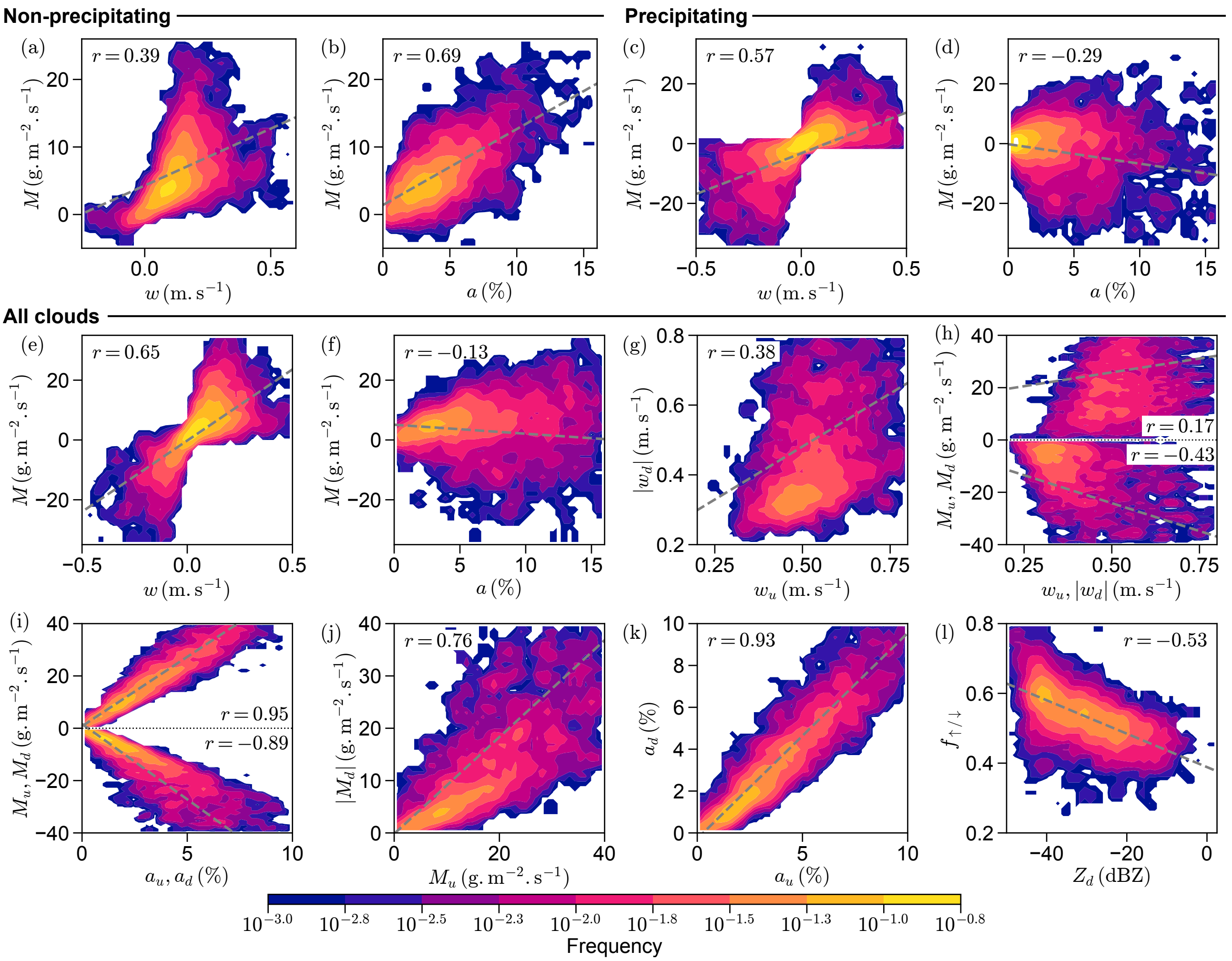

Figure 9. Controls of the cloud base mass fluxes. All variables are taken as their 600 to 900 m average. Relationships are plotted as joint density plots in logarithmic scale for readability. Non-precipitating clouds: (a-b), precipitating clouds: (c-d), all clouds: (e-l). Dashed gray lines and r values report the ordinary linear regression on the underlying data. (a) [resp. (c)] Cloud base mass flux as a function of the cloud base vertical velocity for non-precipitating [resp. precipitating] clouds only. (b) [resp. (d)] Mass flux as a function of the cloud fraction for non-precipitating [resp. precipitating] clouds only. (e) Mass flux as a function of the cloud base vertical velocity. (f) Mass flux as a function of the cloud fraction. (g) Upward velocity as a function of the downward velocity. (h) Upward [resp. downward] mass flux as a function of the upward [resp. downward] velocity. (i) Upward [resp. downward] mass flux as a function of the upward [resp. downward] motion fraction. (j) Downward mass flux as a function of the upward mass flux. (k) Downward motion fraction as a function of the upward motion fraction. (l) Relative updraft-to-downdraft fraction as a function of the cloud base reflectivity.

clouds (Figure 9c, d): the correlation is actually higher between M and w ($r = 0.57$) than between M and a ($r = -0.29$), due to the presence of potentially large downdrafts regardless of the cloud fraction. Large cloud fractions are associated with large magnitudes of M ($r = 0.59$ between a and the absolute value $|M|$, not shown), but the sign of the velocity decides the direction of mass transport. This means that for all clouds overall (Figure 9e, f), M is more controlled by w ($r = 0.65$) than the total cloud fraction ($r = -0.13$). However, when looking at the updraft and downdraft fluxes M_u, M_d separately, the control by the area becomes apparent again: there is weak correlation with the velocities ($r[w_u, M_u] = 0.17$, $r[w_d, M_d] = -0.43$), but high correlation with their areas ($r[a_u, M_u] = 0.95$ and $r[a_d, M_d] = -0.89$). M_u and M_d are themselves closely related ($r = 0.76$), mostly because the updraft and downdraft areas are also strongly related to each other ($r = 0.93$).

The overall mass flux then depends on how M_u and M_d balance out each other. This variability is in part controlled by the amount of precipitation, for which the cloud base reflectivity inside downdrafts Z_d is a proxy (Figure 9l). More precipitation is associated with larger downdrafts (lower $f_{\uparrow/\downarrow}$), which in turn creates larger downward mass flux. While a large M_u is needed to produced a large amount of rain in the first place ($r[Z_d, M_u] = 0.40$, not shown), the rain amount then more tightly controls M_d ($r[Z_d, M_d] = -0.65$, not shown). Overall, when the precipitation amount is high enough, the downdraft may be large enough to outcompete the updraft and the total mass flux ends up being negative ($r[Z_d, M] = -0.49$, not shown).

This mechanism is in line with the precipitation generation argument (Trapp et al., 2017; Marion and Trapp, 2019). The downdraft mass flux is controlled by the rain that produced it, so that rain over a larger area leads to a wider downdraft. The rain area itself depends upon the updraft area that produced it, so that overall, updraft area controls downdraft mass flux, their velocities only playing a secondary role. In non-precipitating clouds, a very similar and robust relationship holds between a_d and a_u, with $a_d \simeq 0.75a_u$ (Figure S7). However, the driving mechanism of these non-precipitating downdrafts is different: they are simply outflows of the convective core, as also seen by the fact that updraft and downdraft velocities correlate well ($r = 0.50$, Figure S7). More frequent thermals generate in equal proportions their smaller subsiding shells, whose strength is set by the updraft strength, leading to the linearities observed. With the action of rain, updrafts are able to generate downdrafts of equal if not larger sizes, with $a_d \simeq 1.1a_u$ (Figure S8). The downdraft velocities are much more decoupled from their parent updrafts velocities ($r = 0.34$), suggesting that it is mostly rain evaporation that sets their strength. This compensating effect means that the cloud fraction alone captures most of the variability in M_u and M_d, but very little of the total M, which is mainly controlled by microphysical variability in the downdrafts. We summarize these results with the very simplified tentative parametrization

$$M_u = \rho w_c a \tag{7}$$

$$M_d = -\rho w_c a \tag{8}$$

$$w_c = 0.27\,\mathrm{m/s} \tag{9}$$

with $R^2 = 0.84$ for M_u and $R^2 = 0.70$ for M_d. The total mass flux is then roughly

$$M = \rho w_u a - \rho w_d a Z_d^{0.06} \tag{10}$$

$$w_u = 0.89\,\mathrm{m/s} \tag{11}$$

$$w_d = 1.29\,\mathrm{m/s} \tag{12}$$

https://doi.org/10.5194/egusphere-2026-1974
Preprint. Discussion started: 15 April 2026

with $R^2 = 0.46$, Z_d being the linear reflectivity in $\mathrm{mm}^6.\mathrm{m}^{-3}$. Note that M_u and M_d sum up to zero, and not M. From the point of view of the subcloud layer, this is not very problematic, as their actions are not symmetric. M_u transports warm and moist subcloud layer air upwards, while M_d brings dry and cold free tropospheric air down. The height of the subcloud layer is set through mass conservation by the total mass flux M (De Szoeke et al., 2017; Naumann et al., 2019; Albright et al., 2023).

Previous observations of shallow, non-precipitating cumuli explain the mass flux variability either by the cloud fraction variability (Klingebiel et al., 2021) or the subcloud layer turbulent kinetic energy (Zheng et al., 2021; Vogel and Mellado, 2025). We believe that the two are not necessarily contradictory. Due to our long record and the fact that we include precipitation, we have nearly twice the variability in cloud fraction during our entire period as was observed during the EUREC^{4}A campaign (mean $\pm 1\sigma$: $2-17\,\%$ in our observations, compared to $2-9\,\%$ in (Vogel et al., 2022)). Since active shallow cumuli sit atop a few thermals (Bony et al., 2025) and they vary less in convective velocity w_c than in cloud fraction, a larger cloud fraction simply implies the existence of more active clouds, all of similar velocities, and thus a larger mass flux. We speculate that the variability in w_c and a due to subcloud layer turbulence could be easier to capture on shorter observational time scales, explaining the apparent discrepancy.

5 Conclusions

We use six years of cloud-profiling radar and Doppler lidar data at the Barbados Cloud Observatory to retrieve the vertical velocity profile in precipitating cumulus clouds in the trades. The retrieval samples the motion of cloud droplets at the edge of the radar Doppler spectrum. It then corrects for turbulent broadening and for the apparent displacement of the cloud cloud droplet velocity by the signal-to-noise-ratio. The radar-retrieved wind is validated against lidar measurements and robust in most conditions.

We show that convective motion intensifies as the clouds deepen over their lifetimes. In non-precipitating cumuli, downward motion is limited to the subsiding shell around the updraft core. In precipitating clouds, when the clouds reach depths near the trade inversion, the rain amount becomes large enough to trigger wide downdrafts. Precipitating clouds act as shallow squall lines: their downdrafts evaporate and form a cold pool at the surface, which strengthens the updraft now triggered at the gust front feeding the precipitation.

In precipitating cumuli, the updraft and the downdraft mass fluxes at cloud base are well-explained by the cloud-base cloud fraction, but they are nearly equal and opposite. Thus cloud fraction bears little relationship with the total mass flux, whose variability is controlled by the variability in the downdraft size and strength due to microphysical effects.

Our results are qualitatively in line with large-eddy simulations of the trades (Li et al., 2014; Dauhut et al., 2023; Alinaghi et al., 2025) and global cloud resolving models (Windmiller et al., 2023). However, what exactly controls the downdraft strength remains unclear. Environmental conditions, such as the lapse rate and relative humidity, and microphysics, are expected to play a role as the drivers of evaporation (Srivastava, 1985; Torri and Kuang, 2016; Windmiller et al., 2023; El Rafei et al., 2025; Sarkar et al., 2025; Niebaum et al., 2025). Since our observations include the EUREC^{4}A and ORCESTRA field campaigns (Stevens et al., 2021; Stevens, 2026), in future work we will use these periods to study the effect of large-scale seasonal environmental conditions on the downdrafts. Microphysical retrievals can leverage the W-band cloud radar at the BCO for dual-frequency applications to reliably estimate the drop size distribution and the evaporation rate (Tridon and Battaglia, 2015; Tridon et al., 2017).

This long-term observational record of in-cloud dynamics can help constrain cloud-resolving models, since it goes beyond the thermodynamic state of the atmosphere or the morphology of the cloud field (Schulz and Stevens, 2023; Raghunathan et al., 2025). Likewise, it can bring new understanding to the basic assumptions behind convective parameterizations. These conceptual models represent deep convective clouds through their mass flux, and often assume a simple proportional relationship between the downdraft and the updraft mass flux, and shallow clouds are treated as non-precipitating (Emanuel, 2019; Tiedtke, 1993; Bechtold et al., 2004; Kain and Fritsch, 1993). We have shown that this approximation is valid, but the precipitation efficiency should be thought of as a function of the rain amount. Our study shows that shallow convection driven by rain processes is very similar at the cloud scale to the dynamics of deep convective systems.

Code and data availability. The code and the data that support the findings of this study are openly available in Zenodo at http://doi.org/10.5281/zenodo.19221500, reference number 19221500. Access to primary Barbados Cloud Observatory data is provided here: https://tcodata.mpimet.mpg.de.

Appendix A: Expanded methods

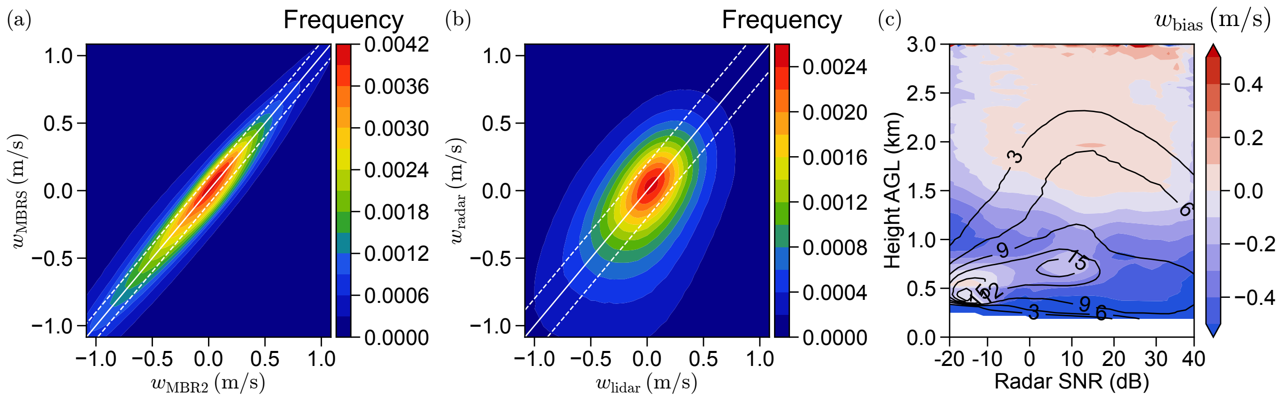

Figure A1. (a) Joint histogram of the MBRS-MBR2 retrieved velocities during the period of joint operation from March 2023 to March 2024. (b) Joint histogram of wind lidar velocity and retrieved velocity from the radar at cloud base. (c) Average pixel-based vertical velocity difference between lidar measurements and the radar retrieval $w_{\mathrm{bias}} = w_{\mathrm{radar}} - w_{\mathrm{lidar}}$, by height and binned by radar SNR. Solid black contour lines: number of pixels by 10000.

Table A1. Table showing the descriptive statistics of the different cloud populations segmented and sampled.

Cloud designation	Thresholds	Counts	Duration mean, median ± IQR (min)	Base height mean, median ± IQR (m)	Top height mean, median ± IQR (m)
Non-precipitating	$Z < -15\,\mathrm{dBZ}$ at all pixels	653559	$0.8, 0.4 \pm 0.7$	$904, 686 \pm 312$	$1075, 873 \pm 468$
Precipitating	$Z > -15\,\mathrm{dBZ}$ in at least one pixel	27363	$12.6, 6.0 \pm 11.2$	$604, 281 \pm 530$	$2033, 2027 \pm 1060$
Precipitating with near-surface echoes	$Z > -15\,\mathrm{dBZ}$ in at least one pixel, cloud base below 250 m	13463	$18.9, 10.5 \pm 13.5$	$166, 156 \pm 0$	$2249, 2245 \pm 967$

Author contributions. FP and RV designed the study. FP performed the analyses and wrote the manuscript. FP and NRB wrote the code. ZZ provided guidance with the retrieval. All the co-authors contributed to the interpretation of the results and commented on the manuscript.

Competing interests. Some authors are members of the editorial board of journal Atmospheric Chemistry and Physics.

Acknowledgements. Many thanks go the Tropical Cloud Observations group at the Max Planck Institute for Meteorology for maintaining the BCO since 2010, to Bjorn Stevens, Friedhelm Jansen, Björn Brügmann, David Farrell and Marvin Forde. Special thanks go to Lutz Hirsch, who provided scientific and technical support regarding the radar data, and to Ilya Serikov and Kirill Viting for maintaining the lidars.

Financial support. F. Poydenot and R. Vogel acknowledge funding from the Deutsche Forschungsgemeinschaft (DFG, German Research Foundation) under Germany's Excellence Strategy - EXC 2037 "Climate, Climatic Change, and Society" (project number 390683824). N. Robbins-Blanch and R. Vogel acknowledge support from an ERC starting grant (ROTOR, grant no. 101116282). Z. Zhu's contribution is funded by the U.S. Department of Energy (DOE) as part of the Atmospheric System Research (ASR) program under Contract DE-SC0012704. This work used resources of the Deutsches Klimarechenzentrum (DKRZ) granted by its Scientific Steering Committee (WLA) under project ID um1487.

https://doi.org/10.5194/egusphere-2026-1974
Preprint. Discussion started: 15 April 2026

References

Acquistapace, C., Schnitt, S., Krause, S., Risse, N., Lange, D., and Chatterjee, D.: Characterizing Trade-Wind Shallow Convection Regimes in the Open Sea with a Synergy of Ship-Based Vertical Profiling Observations, Quarterly Journal of the Royal Meteorological Society, n/a, e70 038, https://doi.org/10.1002/qj.70038, 2026.

Albright, A. L., Stevens, B., Bony, S., and Vogel, R.: A New Conceptual Picture of the Trade Wind Transition Layer, Journal of the Atmospheric Sciences, 80, 1547–1563, https://doi.org/10.1175/JAS-D-22-0184.1, 2023.

Alinaghi, P., Jansson, F., Blázquez, D. A., and Glassmeier, F.: Cold Pools Mediate Mesoscale Adjustments of Trade-Cumulus Fields to Changes in Cloud Droplet Number Concentration, Atmospheric Chemistry and Physics, 25, 6121–6139, https://doi.org/10.5194/acp-25-6121-2025, 2025.

Arakawa, A. and Schubert, W. H.: Interaction of a Cumulus Cloud Ensemble with the Large-Scale Environment, Part I, Journal of the Atmospheric Sciences, 31, 674–701, https://doi.org/10.1175/1520-0469(1974)031<0674:IOACCE>2.0.CO;2, 1974.

Battaglia, A., Mroz, K., Lang, T., Tridon, F., Tanelli, S., Tian, L., and Heymsfield, G. M.: Using a Multiwavelength Suite of Microwave Instruments to Investigate the Microphysical Structure of Deep Convective Cores, Journal of Geophysical Research: Atmospheres, 121, 9356–9381, https://doi.org/10.1002/2016JD025269, 2016.

Battan, L. J. and Theiss, J. B.: Observations of Vertical Motions and Particle Sizes in a Thunderstorm, Journal of the Atmospheric Sciences, 23, 78–87, https://doi.org/10.1175/1520-0469(1966)023<0078:OOVMAP>2.0.CO;2, 1966.

Bechtold, P., Chaboureau, J.-P., Beljaars, A., Betts, A. K., Köhler, M., Miller, M., and Redelsperger, J.-L.: The Simulation of the Diurnal Cycle of Convective Precipitation over Land in a Global Model, Quarterly Journal of the Royal Meteorological Society, 130, 3119–3137, https://doi.org/10.1256/qj.03.103, 2004.

Bony, S., Poujol, B., McKim, B., Rochetin, N., Lothon, M., Windmiller, J., Maury, N., Dufaux, C., Jaffeux, L., Chazette, P., and Delanoë, J.: Evidence for the Role of Thermal and Cloud Merging in Mesoscale Convective Organization, Atmospheric Chemistry and Physics, 25, 17 331–17 362, https://doi.org/10.5194/acp-25-17331-2025, 2025.

Borque, P., Luke, E., and Kollias, P.: On the Unified Estimation of Turbulence Eddy Dissipation Rate Using Doppler Cloud Radars and Lidars, Journal of Geophysical Research: Atmospheres, 121, 5972–5989, https://doi.org/10.1002/2015JD024543, 2016.

Brueck, M., Nuijens, L., and Stevens, B.: On the Seasonal and Synoptic Time-Scale Variability of the North Atlantic Trade Wind Region and Its Low-Level Clouds, Journal of the Atmospheric Sciences, 72, 1428–1446, https://doi.org/10.1175/JAS-D-14-0054.1, 2015.

Byers, H. R., Braham, R. R., and Bureau, U. S. W.: The Thunderstorm: Report of the Thunderstorm Project, U.S. Government Printing Office, 1949.

Dauhut, T., Couvreux, F., Bouniol, D., Beucher, F., Volkmer, L., Pörtge, V., Schäfer, M., Ayet, A., Brilouet, P.-E., Jacob, M., and Wirth, M.: Flower Trade-Wind Clouds Are Shallow Mesoscale Convective Systems, Quarterly Journal of the Royal Meteorological Society, 149, 325–347, https://doi.org/10.1002/qj.4409, 2023.

De Szoeke, S. P., Skyllingstad, E. D., Zuidema, P., and Chandra, A. S.: Cold Pools and Their Influence on the Tropical Marine Boundary Layer, Journal of the Atmospheric Sciences, 74, 1149–1168, https://doi.org/10.1175/JAS-D-16-0264.1, 2017.

El Rafei, M., Isaza, A., Sherwood, S. C., Evans, J., Brown, A., Ji, F., and Dowdy, A.: Downdrafts and Convective Gusts in High-Resolution Simulations: An Australian Case Study, Journal of Geophysical Research: Atmospheres, 130, e2025JD044 151, https://doi.org/10.1029/2025JD044151, 2025.

Emanuel, K.: Inferences from Simple Models of Slow, Convectively Coupled Processes, Journal of the Atmospheric Sciences, 76, 195–208, https://doi.org/10.1175/JAS-D-18-0090.1, 2019.

Emanuel, K. A.: A Scheme for Representing Cumulus Convection in Large-Scale Models, Journal of the Atmospheric Sciences, 48, 2313–2329, https://doi.org/10.1175/1520-0469(1991)048<2313:ASFRCC>2.0.CO;2, 1991.

Frisch, A. S., Fairall, C. W., and Snider, J. B.: Measurement of Stratus Cloud and Drizzle Parameters in ASTEX with a Kα-Band Doppler Radar and a Microwave Radiometer, Journal of the Atmospheric Sciences, 52, 2788–2799, https://doi.org/10.1175/1520-0469(1995)052<2788:MOSCAD>2.0.CO;2, 1995.

Ghate, V. P., Miller, M. A., and DiPretore, L.: Vertical Velocity Structure of Marine Boundary Layer Trade Wind Cumulus Clouds, Journal of Geophysical Research: Atmospheres, 116, https://doi.org/10.1029/2010JD015344, 2011.

Görsdorf, U., Lehmann, V., Bauer-Pfundstein, M., Peters, G., Vavriv, D., Vinogradov, V., and Volkov, V.: A 35-GHz Polarimetric Doppler Radar for Long-Term Observations of Cloud Parameters—Description of System and Data Processing, Journal of Atmospheric and Oceanic Technology, 32, 675–690, https://doi.org/10.1175/JTECH-D-14-00066.1, 2015.

Helfer, K. C. and Nuijens, L.: The Morphology of Simulated Trade-Wind Convection and Cold Pools Under Wind Shear, Journal of Geophysical Research: Atmospheres, 126, e2021JD035 148, https://doi.org/10.1029/2021JD035148, 2021.

Helfer, K. C., Nuijens, L., de Roode, S. R., and Siebesma, A. P.: How Wind Shear Affects Trade-wind Cumulus Convection, Journal of Advances in Modeling Earth Systems, 12, e2020MS002 183, https://doi.org/10.1029/2020MS002183, 2020.

Hernández Pardo, L., Morrison, H., and Possner, A.: Dynamics of Downdrafts Around a Growing Convective Cloud: A Numerical Study, Journal of Geophysical Research: Atmospheres, 130, e2025JD044 236, https://doi.org/10.1029/2025JD044236, 2025.

Heus, T. and Jonker, H. J. J.: Subsiding Shells around Shallow Cumulus Clouds, Journal of the Atmospheric Sciences, 65, 1003–1018, https://doi.org/10.1175/2007JAS2322.1, 2008.

Heus, T., J. Pols, C. F., J. Jonker, H. J., A. Van den Akker, H. E., and H. Lenschow, D.: Observational validation of the compensating mass flux through the shell around cumulus clouds, Quarterly Journal of the Royal Meteorological Society, 135, 101–112, https://doi.org/10.1002/qj.358, 2009.

Houze, R. A.: Structure and Dynamics of a Tropical Squall–Line System, Monthly Weather Review, 105, 1540–1567, https://doi.org/10.1175/1520-0493(1977)105<1540:SADOAT>2.0.CO;2, 1977.

Houze, R. A.: 100 Years of Research on Mesoscale Convective Systems, Meteorological Monographs, 59, 17.1–17.54, https://doi.org/10.1175/AMSMONOGRAPHS-D-18-0001.1, 2018.

Houze, R. A., Cheng, C.-P., Leary, C. A., and Gamache, J. F.: Diagnosis of Cloud Mass and Heat Fluxes from Radar and Synoptic Data, Journal of the Atmospheric Sciences, 37, 754–773, https://doi.org/10.1175/1520-0469(1980)037<0754:DOCMAH>2.0.CO;2, 1980.

Janssens, M., de Arellano, J. V.-G., van Heerwaarden, C. C., de Roode, S. R., Siebesma, A. P., and Glassmeier, F.: Nonprecipitating Shallow Cumulus Convection Is Intrinsically Unstable to Length Scale Growth, Journal of the Atmospheric Sciences, 80, 849–870, https://doi.org/10.1175/JAS-D-22-0111.1, 2023.

Jeong, J.-H., Witte, M. K., Glenn, I. B., Smalley, M., Lebsock, M. D., Lamer, K., and Zhu, Z.: Distinct Dynamical and Structural Properties of Marine Stratocumulus and Shallow Cumulus Clouds in the Eastern North Atlantic, Journal of Geophysical Research: Atmospheres, 127, e2022JD037 021, https://doi.org/10.1029/2022JD037021, 2022.

Kain, J. S. and Fritsch, J. M.: Convective Parameterization for Mesoscale Models: The Kain-Fritsch Scheme, in: The Representation of Cumulus Convection in Numerical Models, edited by Emanuel, K. A. and Raymond, D. J., pp. 165–170, American Meteorological Society, Boston, MA, ISBN 978-1-935704-13-3, https://doi.org/10.1007/978-1-935704-13-3_16, 1993.

Kalesse-Los, H., Kötsche, A., Foth, A., Röttenbacher, J., Vogl, T., and Witthuhn, J.: The Virga-Sniffer – a New Tool to Identify Precipitation Evaporation Using Ground-Based Remote-Sensing Observations, Atmospheric Measurement Techniques, 16, 1683–1704, https://doi.org/10.5194/amt-16-1683-2023, 2023.

Klingebiel, M., Konow, H., and Stevens, B.: Measuring Shallow Convective Mass Flux Profiles in the Trade Wind Region, Journal of the Atmospheric Sciences, 78, 3205–3214, https://doi.org/10.1175/JAS-D-20-0347.1, 2021.

Kollias, P., Albrecht, B. A., and Marks, F.: Why Mie?: Accurate Observations of Vertical Air Velocities and Raindrops Using a Cloud Radar, Bulletin of the American Meteorological Society, 83, 1471–1484, https://doi.org/10.1175/BAMS-83-10-1471, 2002.

Konow, H.: BCO Cloudmask Code, Zenodo, https://doi.org/10.5281/zenodo.4312818, 2020.

Lamaakel, O. and Matheou, G.: Organization Development in Precipitating Shallow Cumulus Convection: Evolution of Turbulence Characteristics, Journal of the Atmospheric Sciences, 79, 2419–2433, https://doi.org/10.1175/JAS-D-21-0334.1, 2022.

Lamer, K. and Kollias, P.: Observations of Fair-Weather Cumuli over Land: Dynamical Factors Controlling Cloud Size and Cover, Geophysical Research Letters, 42, 8693–8701, https://doi.org/10.1002/2015GL064534, 2015.

LeMone, M. A. and Zipser, E. J.: Cumulonimbus Vertical Velocity Events in GATE. Part I: Diameter, Intensity and Mass Flux, Journal of the Atmospheric Sciences, 37, 2444–2457, https://doi.org/10.1175/1520-0469(1980)037<2444:CVVEIG>2.0.CO;2, 1980.

Lhermitte, R. M.: Observation of Rain at Vertical Incidence with a 94 GHz Doppler Radar: An Insight on Mie Scattering, Geophysical Research Letters, 15, 1125–1128, https://doi.org/10.1029/GL015i010p01125, 1988.

Li, Z., Zuidema, P., and Zhu, P.: Simulated Convective Invigoration Processes at Trade Wind Cumulus Cold Pool Boundaries, Journal of the Atmospheric Sciences, 71, 2823–2841, https://doi.org/10.1175/JAS-D-13-0184.1, 2014.

Liu, Y., Geerts, B., Miller, M., Daum, P., and McGraw, R.: Threshold Radar Reflectivity for Drizzling Clouds, Geophysical Research Letters, 35, https://doi.org/10.1029/2007GL031201, 2008.

Malkus, J. S.: On the Formation and Structure of Downdrafts in Cumulus Clouds, Journal of the Atmospheric Sciences, 12, 350–354, https://doi.org/10.1175/1520-0469(1955)012<0350:OTFASO>2.0.CO;2, 1955.

Marion, G. R. and Trapp, R. J.: The Dynamical Coupling of Convective Updrafts, Downdrafts, and Cold Pools in Simulated Supercell Thunderstorms, Journal of Geophysical Research: Atmospheres, 124, 664–683, https://doi.org/10.1029/2018JD029055, 2019.

Medeiros, B. and Nuijens, L.: Clouds at Barbados Are Representative of Clouds across the Trade Wind Regions in Observations and Climate Models, Proceedings of the National Academy of Sciences, 113, https://doi.org/10.1073/pnas.1521494113, 2016.

Moisseev, D. N. and Chandrasekar, V.: Nonparametric Estimation of Raindrop Size Distributions from Dual-Polarization Radar Spectral Observations, Journal of Atmospheric and Oceanic Technology, 24, 1008–1018, https://doi.org/10.1175/JTECH2024.1, 2007.

Narenpitak, P., Kazil, J., Yamaguchi, T., Quinn, P. K., and Feingold, G.: The Sugar-To-Flower Shallow Cumulus Transition Under the Influences of Diel Cycle and Free-Tropospheric Mineral Dust, Journal of Advances in Modeling Earth Systems, 15, e2022MS003 228, https://doi.org/10.1029/2022MS003228, 2023.

Naumann, A. K., Stevens, B., and Hohenegger, C.: A Moist Conceptual Model for the Boundary Layer Structure and Radiatively Driven Shallow Circulations in the Trades, Journal of the Atmospheric Sciences, 76, 1289–1306, https://doi.org/10.1175/JAS-D-18-0226.1, 2019.

Neggers, R., Stevens, B., and Neelin, J. David.: A Simple Equilibrium Model for Shallow-Cumulus-Topped Mixed Layers, Theoretical and Computational Fluid Dynamics, 20, 305–322, https://doi.org/10.1007/s00162-006-0030-1, 2006.

Niebaum, N., Bayley, C. J. A., Poydenot, F., Naumann, A. K., Sarkar, M., and Vogel, R.: Constraining Rain Evaporation from Shallow-Clouds in the Trades Using an Observation-Based Superdroplet Model, EGUsphere, pp. 1–30, https://doi.org/10.5194/egusphere-2025-5551, 2025.

Nuijens, L., Serikov, I., Hirsch, L., Lonitz, K., and Stevens, B.: The Distribution and Variability of Low-level Cloud in the North Atlantic Trades, Quarterly Journal of the Royal Meteorological Society, 140, 2364–2374, https://doi.org/10.1002/qj.2307, 2014.

Nuijens, L., Emanuel, K., Masunaga, H., and L'Ecuyer, T.: Implications of Warm Rain in Shallow Cumulus and Congestus Clouds for Large-Scale Circulations, in: Shallow Clouds, Water Vapor, Circulation, and Climate Sensitivity, edited by Pincus, R., Winker, D., Bony, S., and Stevens, B., pp. 85–110, Springer International Publishing, Cham, ISBN 978-3-319-77273-8, https://doi.org/10.1007/978-3-319-77273-8_5, 2018.

Päschke, E., Leinweber, R., and Lehmann, V.: An Assessment of the Performance of a 1.5 μm Doppler Lidar for Operational Vertical Wind Profiling Based on a 1-Year Trial, Atmospheric Measurement Techniques, 8, 2251–2266, https://doi.org/10.5194/amt-8-2251-2015, 2015.

Raghunathan, G. N., Blossey, P., Boeing, S., Denby, L., Ghazayel, S., Heus, T., Kazil, J., and Neggers, R.: Flower-Type Organized Trade-Wind Cumulus: A Multi-Day Lagrangian Large Eddy Simulation Intercomparison Study, Journal of Advances in Modeling Earth Systems, 17, e2024MS004 864, https://doi.org/10.1029/2024MS004864, 2025.

Rémillard, J. and Tselioudis, G.: Cloud Regime Variability over the Azores and Its Application to Climate Model Evaluation, Journal of Climate, 28, 9707–9720, https://doi.org/10.1175/JCLI-D-15-0066.1, 2015.

Roschke, J., Witthuhn, J., Klingebiel, M., Haarig, M., Foth, A., Kötsche, A., and Kalesse-Los, H.: Discriminating between "Drizzle or Rain" and Sea Salt Aerosols in Cloudnet for Measurements over the Barbados Cloud Observatory, Atmospheric Measurement Techniques, 18, 487–508, https://doi.org/10.5194/amt-18-487-2025, 2025.

Rotunno, R., Klemp, J. B., and Weisman, M. L.: A Theory for Strong, Long-Lived Squall Lines, Journal of the Atmospheric Sciences, 45, 463–485, https://doi.org/10.1175/1520-0469(1988)045<0463:ATFSLL>2.0.CO;2, 1988.

Sarkar, M., Vogel, R., and Zheng, Y.: Microphysics Dominates Sub-Cloud Rain Evaporation in Trade Cumuli Over Barbados, Geophysical Research Letters, 52, e2025GL114 885, https://doi.org/10.1029/2025GL114885, 2025.

Schulz, H. and Stevens, B.: Evaluating Large-Domain, Hecto-Meter, Large-Eddy Simulations of Trade-Wind Clouds Using EUREC4A Data, Journal of Advances in Modeling Earth Systems, 15, e2023MS003 648, https://doi.org/10.1029/2023MS003648, 2023.

Schulz, H., Eastman, R., and Stevens, B.: Characterization and Evolution of Organized Shallow Convection in the Downstream North Atlantic Trades, Journal of Geophysical Research: Atmospheres, 126, e2021JD034 575, https://doi.org/10.1029/2021JD034575, 2021.

Seifert, A. and Heus, T.: Large-Eddy Simulation of Organized Precipitating Trade Wind Cumulus Clouds, Atmospheric Chemistry and Physics, 13, 5631–5645, https://doi.org/10.5194/acp-13-5631-2013, 2013.

Shupe, M. D., Kollias, P., Poellot, M., and Eloranta, E.: On Deriving Vertical Air Motions from Cloud Radar Doppler Spectra, Journal of Atmospheric and Oceanic Technology, 25, 547–557, https://doi.org/10.1175/2007JTECHA1007.1, 2008.

Srivastava, R. C.: A Simple Model of Evaporatively Driven Downdraft: Application to Microburst Downdraft, Journal of the Atmospheric Sciences, 42, 1004–1023, https://doi.org/10.1175/1520-0469(1985)042<1004:ASMOED>2.0.CO;2, 1985.

Stevens, B.: ORCESTRA, https://orcestra-campaign.org/orcestra.html, 2026.

Stevens, B., Farrell, D., Hirsch, L., Jansen, F., Nuijens, L., Serikov, I., Brügmann, B., Forde, M., Linne, H., Lonitz, K., and Prospero, J. M.: The Barbados Cloud Observatory: Anchoring Investigations of Clouds and Circulation on the Edge of the ITCZ, Bulletin of the American Meteorological Society, 97, 787–801, https://doi.org/10.1175/BAMS-D-14-00247.1, 2016.

Stevens, B., Bony, S., Farrell, D., Ament, F., Blyth, A., Fairall, C., Karstensen, J., Quinn, P. K., Speich, S., Acquistapace, C., Aemisegger, F., Albright, A. L., Bellenger, H., Bodenschatz, E., Caesar, K.-A., Chewitt-Lucas, R., de Boer, G., Delanoë, J., Denby, L., Ewald, F., Fildier, B., Forde, M., George, G., Gross, S., Hagen, M., Hausold, A., Heywood, K. J., Hirsch, L., Jacob, M., Jansen, F., Kinne, S., Klocke, D., Kölling, T., Konow, H., Lothon, M., Mohr, W., Naumann, A. K., Nuijens, L., Olivier, L., Pincus, R., Pöhlker, M., Reverdin, G., Roberts, G., Schnitt, S., Schulz, H., Siebesma, A. P., Stephan, C. C., Sullivan, P., Touzé-Peiffer, L., Vial, J., Vogel, R., Zuidema, P., Alexander, N., Alves, L., Arixi, S., Asmath, H., Bagheri, G., Baier, K., Bailey, A., Baranowski, D., Baron, A., Barrau, S., Barrett, P. A., Batier, F., Behrendt, A., Bendinger, A., Beucher, F., Bigorre, S., Blades, E., Blossey, P., Bock, O., Böing, S., Bosser, P., Bourras, D., Bouruet-Aubertot, P., Bower, K., Branellec, P., Branger, H., Brennek, M., Brewer, A., Brilouet, P.-E., Brügmann, B., Buehler, S. A., Burke, E., Burton, R., Calmer, R., Canonici, J.-C., Carton, X., Cato Jr., G., Charles, J. A., Chazette, P., Chen, Y., Chilinski, M. T., Choularton, T., Chuang, P., Clarke, S., Coe, H., Cornet, C., Coutris, P., Couvreux, F., Crewell, S., Cronin, T., Cui, Z., Cuypers, Y., Daley, A., Damerell, G. M., Dauhut, T., Deneke, H., Desbios, J.-P., Dörner, S., Donner, S., Douet, V., Drushka, K., Dütsch, M., Ehrlich, A., Emanuel, K., Emmanouilidis, A., Etienne, J.-C., Etienne-Leblanc, S., Faure, G., Feingold, G., Ferrero, L., Fix, A., Flamant, C., Flatau, P. J., Foltz, G. R., Forster, L., Furtuna, I., Gadian, A., Galewsky, J., Gallagher, M., Gallimore, P., Gaston, C., Gentemann, C., Geyskens, N., Giez, A., Gollop, J., Gouirand, I., Gourbeyre, C., de Graaf, D., de Groot, G. E., Grosz, R., Güttler, J., Gutleben, M., Hall, K., Harris, G., Helfer, K. C., Henze, D., Herbert, C., Holanda, B., Ibanez-Landeta, A., Intrieri, J., Iyer, S., Julien, F., Kalesse, H., Kazil, J., Kellman, A., Kidane, A. T., Kirchner, U., Klingebiel, M., Körner, M., Kremper, L. A., Kretzschmar, J., Krüger, O., Kumala, W., Kurz, A., L'Hégaret, P., Labaste, M., Lachlan-Cope, T., Laing, A., Landschützer, P., Lang, T., Lange, D., Lange, I., Laplace, C., Lavik, G., Laxenaire, R., Le Bihan, C., Leandro, M., Lefevre, N., Lena, M., Lenschow, D., Li, Q., Lloyd, G., Los, S., Losi, N., Lovell, O., Luneau, C., Makuch, P., Malinowski, S., Manta, G., Marinou, E., Marsden, N., Masson, S., Maury, N., Mayer, B., Mayers-Als, M., Mazel, C., McGeary, W., McWilliams, J. C., Mech, M., Mehlmann, M., Meroni, A. N., Mieslinger, T., Minikin, A., Minnett, P., Möller, G., Morfa Avalos, Y., Muller, C., Musat, I., Napoli, A., Neuberger, A., Noisel, C., Noone, D., Nordsiek, F., Nowak, J. L., Oswald, L., Parker, D. J., Peck, C., Person, R., Philippi, M., Plueddemann, A., Pöhlker, C., Pörtge, V., Pöschl, U., Pologne, L., Posyniak, M., Prange, M., Quiñones Meléndez, E., Radtke, J., Ramage, K., Reimann, J., Renault, L., Reus, K., Reyes, A., Ribbe, J., Ringel, M., Ritschel, M., Rocha, C. B., Rochetin, N., Röttenbacher, J., Rollo, C., Royer, H., Sadoulet, P., Saffin, L., Sandiford, S., Sandu, I., Schäfer, M., Schemann, V., Schirmacher, I., Schlenczek, O., Schmidt, J., Schröder, M., Schwarzenboeck, A., Sealy, A., Senff, C. J., Serikov, I., Shohan, S., Siddle, E., Smirnov, A., Späth, F., Spooner, B., Stolla, M. K., Szkółka, W., de Szoeke, S. P., Tarot, S., Tetoni, E., Thompson, E., Thomson, J., Tomassini, L., Totems, J., Ubele, A. A., Villiger, L., von Arx, J., Wagner, T., Walther, A., Webber, B., Wendisch, M., Whitehall, S., Wiltshire, A., Wing, A. A., Wirth, M., Wiskandt, J., Wolf, K., Worbes, L., Wright, E., Wulfmeyer, V., Young, S., Zhang, C., Zhang, D., Ziemen, F., Zinner, T., and Zöger, M.: EUREC4A, Earth System Science Data, 13, 4067–4119, https://doi.org/10.5194/essd-13-4067-2021, 2021.

Tiedtke, M.: Representation of Clouds in Large-Scale Models, Monthly Weather Review, 121, 3040–3061, https://doi.org/10.1175/1520-0493(1993)121<3040:ROCILS>2.0.CO;2, 1993.

Torri, G. and Kuang, Z.: A Lagrangian Study of Precipitation-Driven Downdrafts, Journal of the Atmospheric Sciences, 73, 839–854, https://doi.org/10.1175/JAS-D-15-0222.1, 2016.

Touzé-Peiffer, L., Vogel, R., and Rochetin, N.: Cold Pools Observed during EUREC4A: Detection and Characterization from Atmospheric Soundings, Journal of Applied Meteorology and Climatology, 61, 593–610, https://doi.org/10.1175/JAMC-D-21-0048.1, 2022.

Trapp, R. J., Marion, G. R., and Nesbitt, S. W.: The Regulation of Tornado Intensity by Updraft Width, Journal of the Atmospheric Sciences, 74, 4199–4211, https://doi.org/10.1175/JAS-D-16-0331.1, 2017.

Tridon, F. and Battaglia, A.: Dual-Frequency Radar Doppler Spectral Retrieval of Rain Drop Size Distributions and Entangled Dynamics Variables, Journal of Geophysical Research: Atmospheres, 120, 5585–5601, https://doi.org/10.1002/2014JD023023, 2015.

Tridon, F., Battaglia, A., Luke, E., and Kollias, P.: Rain Retrieval from Dual-frequency Radar Doppler Spectra: Validation and Potential for a Midlatitude Precipitating Case-study, Quarterly Journal of the Royal Meteorological Society, 143, 1364–1380, https://doi.org/10.1002/qj.3010, 2017.

Vial, J., Vogel, R., Bony, S., Stevens, B., Winker, D. M., Cai, X., Hohenegger, C., Naumann, A. K., and Brogniez, H.: A New Look at the Daily Cycle of Trade Wind Cumuli, Journal of Advances in Modeling Earth Systems, 11, 3148–3166, https://doi.org/10.1029/2019MS001746, 2019.

Vogel, R. and Mellado, J. P.: Do Observations Support Ideas Behind Common Mass Flux Closures?, Geophysical Research Letters, 52, e2025GL115 545, https://doi.org/10.1029/2025GL115545, 2025.

Vogel, R., Konow, H., Schulz, H., and Zuidema, P.: A Climatology of Trade-Wind Cumulus Cold Pools and Their Link to Mesoscale Cloud Organization, Atmospheric Chemistry and Physics, 21, 16 609–16 630, https://doi.org/10.5194/acp-21-16609-2021, 2021.

Vogel, R., Albright, A. L., Vial, J., George, G., Stevens, B., and Bony, S.: Strong Cloud–Circulation Coupling Explains Weak Trade Cumulus Feedback, Nature, 612, 696–700, https://doi.org/10.1038/s41586-022-05364-y, 2022.

Wang, Y. and Geerts, B.: Composite Vertical Structure of Vertical Velocity in Nonprecipitating Cumulus Clouds, Monthly Weather Review, 141, 1673–1692, https://doi.org/10.1175/MWR-D-12-00047.1, 2013.

Weisman, M. L. and Rotunno, R.: "A Theory for Strong Long-Lived Squall Lines" Revisited, Journal of the Atmospheric Sciences, 61, 361–382, https://doi.org/10.1175/1520-0469(2004)061<0361:ATFSLS>2.0.CO;2, 2004.

Windmiller, J. M., Bao, J., Sherwood, S. C., Schanzer, T. D., and Fuchs, D.: Predicting Convective Downdrafts From Updrafts and Environmental Conditions in a Global Storm Resolving Simulation, Journal of Advances in Modeling Earth Systems, 15, e2022MS003 048, https://doi.org/10.1029/2022MS003048, 2023.

Yurk, N. Y., Lebsock, M. D., Socuellamos, J. M., Rodriguez Monje, R., Cooper, K. B., and Kollias, P.: Vertical Wind and Drop Size Distribution Retrieval with the CloudCube G-band Doppler Radar, Atmospheric Measurement Techniques, 18, 5141–5155, https://doi.org/10.5194/amt-18-5141-2025, 2025.

Zheng, Y., Rosenfeld, D., and Li, Z.: Sub-Cloud Turbulence Explains Cloud-Base Updrafts for Shallow Cumulus Ensembles: First Observational Evidence, Geophysical Research Letters, 48, e2020GL091 881, https://doi.org/10.1029/2020GL091881, 2021.

Zhu, Z., Kollias, P., Yang, F., and Luke, E.: On the Estimation of In-Cloud Vertical Air Motion Using Radar Doppler Spectra, Geophysical Research Letters, 48, e2020GL090 682, https://doi.org/10.1029/2020GL090682, 2021.

Zipser, E. J. and LeMone, M. A.: Cumulonimbus Vertical Velocity Events in GATE. Part II: Synthesis and Model Core Structure, Journal of the Atmospheric Sciences, 37, 2458–2469, https://doi.org/10.1175/1520-0469(1980)037<2458:CVVEIG>2.0.CO;2, 1980.